Primary drivers of multidecadal spatial and temporal patterns of shoreline change derived from optical satellite imagery

Bruno Castelle, Auguste Ritz, Vincent Marieu, Alexandre Nicolae Lerma, Marine Vandenhove

Primary drivers of multidecadal spatial and temporal patterns of shoreline change derived from optical satellite imagery

Bruno Castelle[1,2], Auguste Ritz[1,2], Vincent Marieu[1,2], Alexandre Nicolae Lerma[3,4], Marine Vandenhove[1,2,3]

[1]CNRS, UMR EPOC, Pessac, France

[2]Université de Bordeaux, UMR EPOC, Pessac, France

[3]BRGM French Geological Survey, Regional Direction Nouvelle- Aquitaine, Pessac, France

[4]Observatoire de la Côte Nouvelle Aquitaine (OCNA), Pessac, France

Corresponding author: bruno.castelle@u-bordeaux.fr

Highlights

- 1984-2020 satellite-derived shorelines (SDS) collected along 269 km of sandy coast
- Gradients in longshore drift control shoreline trends away from estuary mouths
- Space-averaged SDS interannual variability is correlated with some climate indices
- Sectors downdrift of inlets and estuary mouths are affected by internal dynamics
- SDS can guide the development and application of shoreline change models

Abstract

Understanding and predicting shoreline change along sandy coasts requires continuous (in both time and space) long-term (decades) shoreline data at good spatial (e.g. 100s of metres) and temporal (e.g. months) resolution. Publicly available satellite imagery can now provide such time series. However, satellite-derived shorelines (SDS) are associated with uncertainties, particularly at high-energy meso-macrotidal coasts, which challenge the assessment of long-term trends and interannual

variability. In this paper we address the 1984-2020 time- and space-evolution of 269 km of high-energy meso-macrotidal sandy coast in southwest France using uncertain (no tide and runup correction) SDS data. The shoreline trends are validated with field data collected over the period 2008-2019. Over 1984-2020, the shoreline eroded by 0.55 m/yr with maximum erosion (accretion) reaching 15.61 m/yr (6.94 m/yr), with the largest changes observed along coasts adjacent to the inlet and estuary mouths. We show that, away from the presence of ebb-tide deltas and swash bars affecting offshore wave transformation and nearshore circulation, the long-term shoreline trend is well explained by the gradients in longshore drift computed from a regional wave hindcast and an empirical longshore transport formula. By averaging the yearly SDS along the entire coastline, we find that interannual shoreline variability is well correlated with the winter West Europe Pressure Anomaly (WEPA), which outscores the other conventional teleconnection pattern indices. WEPA even explains more than 80% of the space-averaged shoreline variability over the recent period 2014-2020 when more and higher quality satellite images are available. A more local assessment of the links between climate indices and shoreline response shows that correlation with all climate indices dramatically drops downdrift of the large-scale estuary mouths and inlets. This suggests that along this 10-20 km stretch of downdrift coast, shoreline response is controlled factors internal to the estuary mouth / inlet system. The rest of the coast is mostly controlled by factors external to the system, which are primarily the variability in winter-mean wave height correlated to winter WEPA index. Overall, we demonstrate that an adapted space-averaging of uncorrected (noisy) SDS dataset can allow addressing the time- and space variability of shoreline change and their primary drivers including large-scale climate patterns of atmospheric variability. We also advocate that such SDS analysis can be performed along any coastline in the world in order to guide future model development and application.

Keywords: satellite-derived shoreline; chronic erosion; interannual shoreline variability; wave climate indices; internal and external controls; inlet and estuary mouth

1. Introduction

Climate change, declining sediment supply, and global population growth in the coastal zone are projected to result in unprecedented socio-economic losses and environmental changes in the coming decades (Oppenheimer et al., 2019). This is particularly the case of sandy beaches (approximately one-third of the global ice-free coastline, Luijendijk et al., 2018) which are highly dynamic and provide outstanding recreation, tourism and ecosystem services, while acting as energy buffers in an increasingly stormy environment. Erosion has therefore become one of the biggest threats to coastal zones globally, both in developed (e.g. Southern California, Vitousek et al., 2017a) and less developed (e.g. North Africa Hzami et al., 2021) regions of the world, which calls for improved understanding of past and future shoreline evolution and its drivers. This motivated the recent development of a wealth of reduced-complexity, computationally cheap, shoreline models (e.g. Vitousek et al., 2017b; Robinet et al., 2018; Antonilez et al., 2019; Tran and Barthélemy, 2020) able to simulate shoreline change on timescales of decades of coastlines extending up to 10s to 100s of kilometres. However, model performance heavily relies on training datasets on similar spatial and temporal scales, and comparisons between multiple models on additional datasets are strongly needed (Montano et al., 2020).

Free-of-charge publicly available optical satellite imagery can now be used to provide short-term to multi-decadal shoreline data from the local to the global scale using different techniques (e.g. Liu et al., 2017; Duarte et al., 2018; Toure et al., 2019; Sánchez-García et al., 2020; Bishop-Taylor et al., 2021). On microtidal beaches, satellite-derived shoreline (SDS) errors are typically under 10 m (e.g. Vos et al., 2019a; Bishop-Taylor et al., 2019; Cuttler et al., 2020). Therefore in such environments SDS can be used to improve the understanding of, for instance, embayed beach rotation (Di Luccio et al., 2019) or the dominant timescales of shoreline variability (Vos et al., 2019a). However, SDS accuracy dramatically worsens at high-energy and/or meso to macrotidal low-gradient beaches with errors

potentially exceeding 30 m (Castelle et al., 2021) due to the action of breaking waves affecting the total water level at the coast and blurring the dry sand / water limit. Recently, Castelle et al. (2021) investigated the uncertainties associated with SDS on a high-energy meso-macrotidal beach in southwest France. They proposed a new total water level threshold accounting for wave runup which, combined with a horizontal correction of shoreline position based on average beach slope estimated from *in situ* data, halves shoreline error (decreasing to around 10 m) and doubles the number of usable satellite images, thus dramatically improving shoreline reconstruction. However, and despite fair remotely-sensed beach slope datasets can now be generated (Vos et al., 2020), long-term breaking wave condition hindcast is challenging to generate and such runup correction ideally needs detailed wave modelling combined with accurate bathymetric data, particularly in complex coastal settings (e.g., sheltered zones, offshore bathymetric anomalies affecting wave transformation).

Global assessment of long-term sandy shoreline trends at 500-m spaced transects has been performed using annual composite of cloud-free images (Luijendijk et al., 2018), i.e. disregarding tide and runup correction. Despite the apparent simplicity of the composite SDS approach (in contrast to the synoptic SDS approach), the spatially-averaged, regional analyses provided fairly accurate insights into chronic shoreline trends for sandy beaches across the globe (Luijendijk et al., 2018). The ability of SDS without tide and runup correction to provide accurate long-term shoreline trends along entire stretches of coast with contrasting evolution pathways has not been fully validated, particularly at high-energy meso-macrotidal environments. In addition, the strong links between interannual shoreline response and large-scale climate patterns of atmospheric variability has been explored only locally, based *in situ* monitoring program (e.g. Dodet et al., 2019). The recent work of Vos *et al*. (2022) is a notable exception, where SDS anomaly around the Pacific Basin was computed during extreme (El Niño/Southern Oscillation) ENSO index phases (multivariate index larger than half of its standard deviation). The authors found significant and coherent regional variability in coastal response to ENSO. The space-averaging of uncorrected (noisy) SDS datasets could, by smoothing the

errors, allow addressing the regional variability of the links between shoreline response and different modes of climate variability. However, this has never been tested.

The southwest coast of France is made of high-energy meso-macrotidal beaches. The coast has been eroding over the last decades although erosion and accretion can alternate in both time and space particularly near large-scale tidal inlets and estuary mouths (Castelle et al., 2018a). So far, continuous large-scale (~250 km) long-term (~70 years) shoreline analysis along this coast has only been performed at low-frequency (~10 years) using historical orthophotos (Bernon et al., 2016; Castelle et al., 2018a), while high-frequency (daily to monthly) data (<20 years) are limited to a couple of sites (e.g. Coco et al., 2014; Biausque and Sénéchal, 2019; Castelle et al., 2020). In this paper 269 km of sandy coast in southwest France are studied using, uncorrected, SDS data from 1984 to 2020. We explore if time- and/or space-averaging of such SDS data can be used to describe shoreline change, including long-term trends and interannual variability, and their primary driver. To do so, we validate the SDS trends with *in situ* data and further use wave hindcast, longshore drift estimations and climate indices to link the observed changes with external forcing. We will show that the processing of such SDS data can provide new insight into shoreline response and their primary, thus indicating guidelines for future model development and application.

2. Study area: the sandy coast of Nouvelle-Aquitaine

The present study focuses on a large sector of the sandy coast of the Nouvelle-Aquitaine region, southwest France, from the mouth of the Adour River in the south to the south of Oléron Island in the north (Figure 1a). The role of the inherited geology on coastline shape and landscape is extensively described in Castelle et al. (2018a). The coast is disrupted by two major inlets (Maumusson and Arcachon), associated with two prominent updrift sandspits (Gatseau and Cap Ferret), and one large estuary mouth (Gironde). The coast is mostly composed of relatively straight sandy beaches backed by coastal dunes (Figure 1d, Bossard and Nicolae Lerma, 2020), with only a few, isolated, coastal towns built on the dune although with limited coastal defences (e.g. Royan,

Soulac, Montalivet, Lacanau, Mimizan, Capbreton, Figure 1a). The coast is also slightly disrupted by the small-scale wave-dominated inlets of Mimizan, Contis-les-Bains, Capbreton and Huchet, with only the latter being not trained by jetties. In the south of the study area, the jetties and groins of the coastal town of Capbreton, the Capbreton submarine canyon, and the northern training wall of the Adour river mouth also disrupt the sediment pathways.

Beaches are made of fine to medium quartz sand slightly coarsening southwards. It is a meso-macrotidal environment with the tidal range increasing northwards due to the widening continental shelf (Le Cann, 1990), with the highest astronomical tide peaking around 6.5 m in the north. The coast is exposed to an energetic wave climate generated by extratropical cyclones tracking eastwards in the North Atlantic Ocean, driving waves predominantly with a west to northwest incidence. While offshore significant wave height H_s can exceed 10 m during severe storms, the monthly-averaged H_s in the centre of the study area ranges from 1.11 m in July to 2.4 m in January (Castelle et al., 2017a). Winter-mean incident wave energy shows dramatic interannual variability enforced by natural large-scale climate modes of atmospheric variability, primarily the West Europe Pressure Anomaly (Castelle et al., 2017b). Overall, the wave height at breaking slightly increases southwards because of the narrowing continental shelf reducing the bottom friction and resulting in less offshore energy dissipation of the incoming ocean waves. The dominant west-northwest wave climate drives a net southerly longshore drift (Bertin et al., 2008; Idier et al., 2013), except locally at northwest-facing sectors where the longshore drift reverses. The longshore drift also locally reverses north of Capbreton owing to offshore wave refraction across the Capbreton canyon (Abadie et al., 2006; Mazieres et al., 2014).

Castelle et al. (2018a) used 15 geo-referenced orthomosaics photos between 1950 to 2014 from which shoreline position was manually retrieved using as proxy the dune foot and the limit of the vegetated foredune in eroding and accreting sectors, respectively. The authors showed that, averaged across the entire sandy coast, the shoreline has eroded by 1.12 m/yr at a relatively steady

rate. Maximum rates of shoreline change are observed along sectors adjacent to the inlets and estuary mouths. In these sectors, erosion and accretion typically alternate over time on the timescale of decades (e.g. Cap Ferret sandspit, Figure 1e). Computed shoreline change rates range from -11 m/yr (+6 m/yr) in eroding (accreting) sectors, which is evidenced by the coastal landscape in rapidly chronically accreting (e.g. Cape Verdon sector, Figure 1b) and eroding (e.g. Cap Négade, Figure 1c) sectors. Although not captured by the, low-frequency, historical orthophoto analysis in Castelle et al. (2018a), observation along the coast also shows occasional dramatic shoreline erosion driven by severe winters. The most striking example is the winter of 2013/2014, characterised by extreme storm clustering (Davies, 2015), which drove widespread erosion along the Atlantic coast of Europe (Masselink et al., 2016), including the southwest coast of France (Castelle et al., 2015).

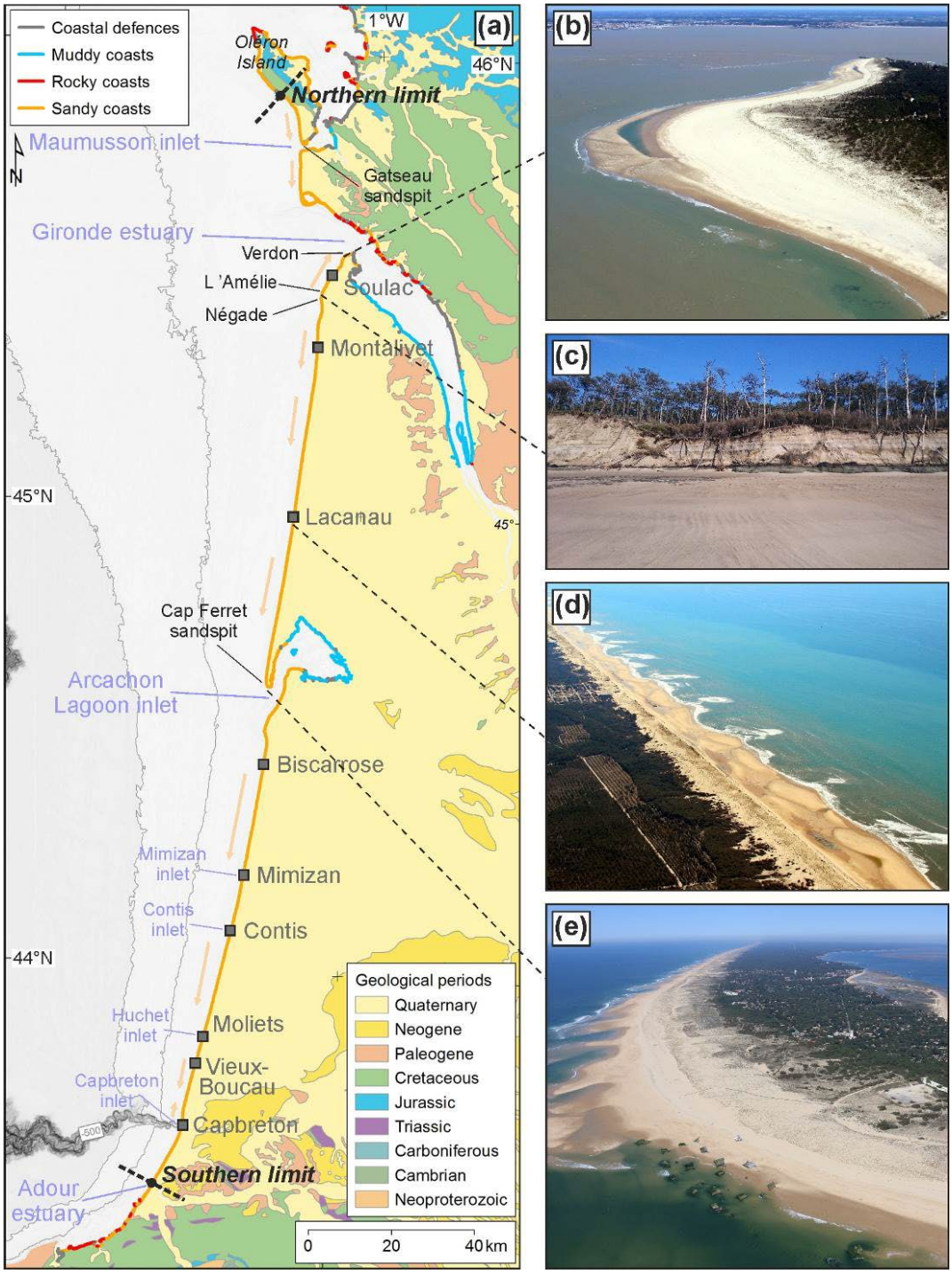

Figure 1. Study area (delimited by the southern and northern black dashed segments) mostly composed of sandy coasts, with indication of the inherited geology. The grey squares show the location of the small coastal towns with their seafront more or less built on the coastal dune, and the alongshore arrows show the net longshore drift patterns. The right-hand photos display some representative coastal settings: (b) accreting sector south of Cape Verdon (@Observatoire de la Côte de Nouvelle-Aquitaine); (c) chronically eroding Cape Négade where the dune has disappeared (Ph.

B. Castelle); (d) typical landscape of long and straight beach-dune systems (@Observatoire de la Côte de Nouvelle-Aquitaine); (e) the tip of the Cap Ferret sandspit, adjacent to the Arcachon Lagoon inlet, which has a long history of alternatively eroding and accreting phases as evidenced by the Second World War German bunkers, formerly built on the top of the coastal dune, now lost to coastal erosion (@Observatoire de la Côte de Nouvelle-Aquitaine).

3. Methods

3.1 *Shoreline detection from publicly available satellite images*

We used the CoastSat toolkit developed by Vos et al. (2019a, 2019b). The toolkit allows extracting waterlines from publicly available optical satellite data through Google Earth Engine, namely Landsat 5, 7 & 8 (L5, L7, L8, 30-m spatial resolution) and Sentinel-2 (S2, 10-m spatial resolution) images. In brief, for a given RGB (+ infrared) satellite image (Figure 2a), image classification into four classes is performed based on a Neural Network classifier (Figure 2b) which, combined with a global threshold on the Modified Normalised Difference Water Index (MNDWI), provides a waterline using a sub-pixel resolution contouring algorithm (Figure 2c). For an extensive description of the CoastSat toolkit, the reader is referred to Vos et al. (2019b). Following Castelle et al. (2021) who used CoastSat at Truc Vert beach on this coast, images with cloud cover larger than 50% were automatically disregarded. Additional images were manually removed by visual inspection when the algorithm failed to depict shoreline position due to e.g. flawed detection of the water/sand limit in the saturated intertidal domain or shadows cast by clouds affecting waterline detection. Contrary to Castelle et al. (2021), tide and runup SDS correction was not performed because accurate runup estimation was not possible at many sectors affected by offshore wave refraction / breaking that strongly affect nearshore breaking wave conditions. Disregarding such correction and thus using off-the-shelf CoastSat toolkit also allowed us to explore if and how spatial or temporal averaging can provide accurate and new information on shoreline change along this coast.

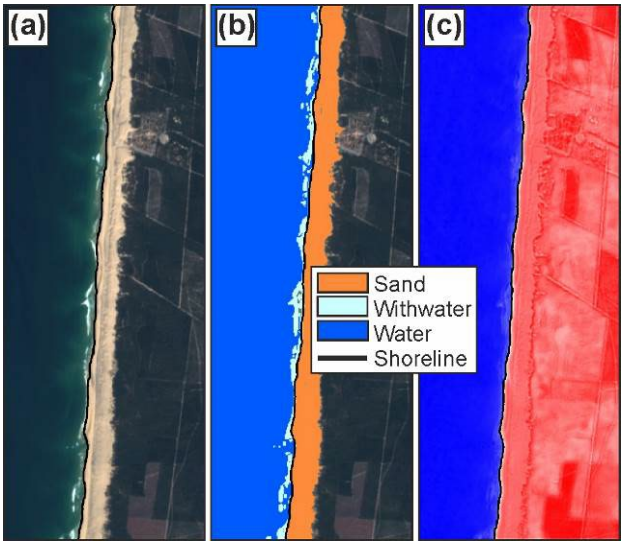

Figure 2. Outputs from the CoastSat toolkit of Vos (2019b): (a) RGB image of a stretch of coast north of Lacanau (S2 on April 18, 2020); (b) corresponding output of image classification where each pixel is labelled as 'sand', 'water', 'white-water' or 'other'; (c) corresponding pseudocolour image of the MNDWI pixel values. In all panels, the black line indicates the waterline detected by CoastSat.

The southwest coast of France was subdivided into boxes to which satellite images were cropped and processed with CoastSat. A total of 126, approximately 20% overlapping, boxes were designed (area ranging from 5.53 km^2 to 14.65 km^2, with a mean of 9.34 km^2) ranging from the Spanish border to the entire Oléron Island (Figure 3a). The resulting 512-km shoreline baseline is made of 1024 500-m-spaced cross-shore transects. Each box contains eight central transects used for analysis (Figure 3b,c), the other transects overlapping those in the two neighbouring boxes. In order to focus on open sandy coast sectors, we disregarded the beaches (1) of the Basque coast south of the Adour River mouth, (2) inside the Arcachon Lagoon, (3) in predominantly muddy, trained or rocky sectors within the Gironde estuary mouth and (4) in Oléron island sectors which are sheltered from ocean waves and/or with thin beaches mostly perched on rocky basement, thus with limited dynamics (Figure 3a). Overall, 269 km of sandy shoreline (538 transects) were analysed, for a total of 104,444 individual shoreline positions between April 12, 1984 and December 31, 2020.

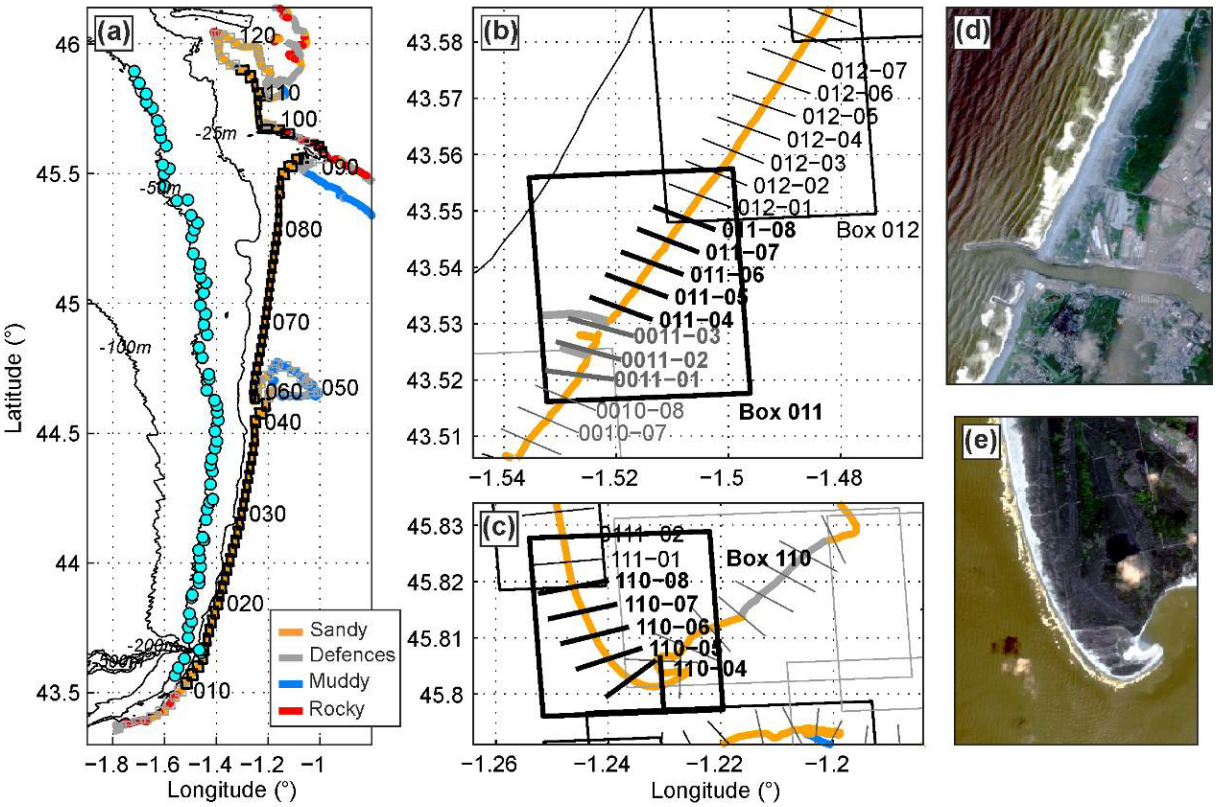

Figure 3. (a) Location map of the southwest coast of France, with colour indicating shoreline type, and with the bathymetry contoured. The boxes (numbered) indicate Coastsat image extraction zones along the entire coast with the cyan dots indicating the corresponding wave hindcast grid points in approximately 50-m depth where wave time series were extracted. The thick black boxes show the boxes used in the present analysis. Middle and right-hand panels show a zoom onto boxes 011 and 110 and examples of corresponding satellite image. (b,c) Each box consists of eight 500-m spaced cross-shore transects, with in each thick black box the greyish transects disregarded from the analysis (e.g. outside of the domain, located in a sheltered area). S2 images on (d) June 22, 2020 and (e) June 13, 2019.

3.2 *Satellite-derived shoreline trend computation and validation*

At each transect, time series of shoreline deviation from the mean was retrieved from the CoastSat-derived shoreline position S. Given that shoreline trends are sometimes based on the entire shoreline time series (e.g. Vos et al., 2019), or sometimes from annual composite images (Luijendijk et al., 2018), two approaches for computing long-term shoreline trends were tested here: by linearly

224 regressing (1) raw S giving trend dS/dt and (2) yearly-mean SDS S_y giving trend dS_y/dt. Figure 4
225 shows examples of S time series at representative transects showing contrasting variability in both
226 pattern and amplitude, e.g. from a quasi-steady erosion (Figure 4b) to strong interannual variability
227 with an amplitude of 100s of metres and net accreting long-term trend (Figure 4d). Trends from the
228 two methods are shown for two different periods, i.e. the entire 1984-2020 time series and for the
229 2008-2019 period which will be used for validation with field data. The two methods show similar
230 results, with a root-mean-square error RMSE and coefficient of determination R^2 of 0.59 m/yr and
231 0.95, respectively, for the 1984-2020 period (Figure 5a), changing to 1.06 m/yr and 0.92 for the 2008-
232 2019 period (Figure 5b). In the following, long-term trend using raw S is used throughout (dS/dt).
233 We also computed the S standard deviation around the long-term trend σ_s, which is composed of all
234 the components of errors and variability, namely : seasonal and particularly interannual variability
235 and SDS detection uncertainties (e.g. shoreline detection algorithm, tide effects) .

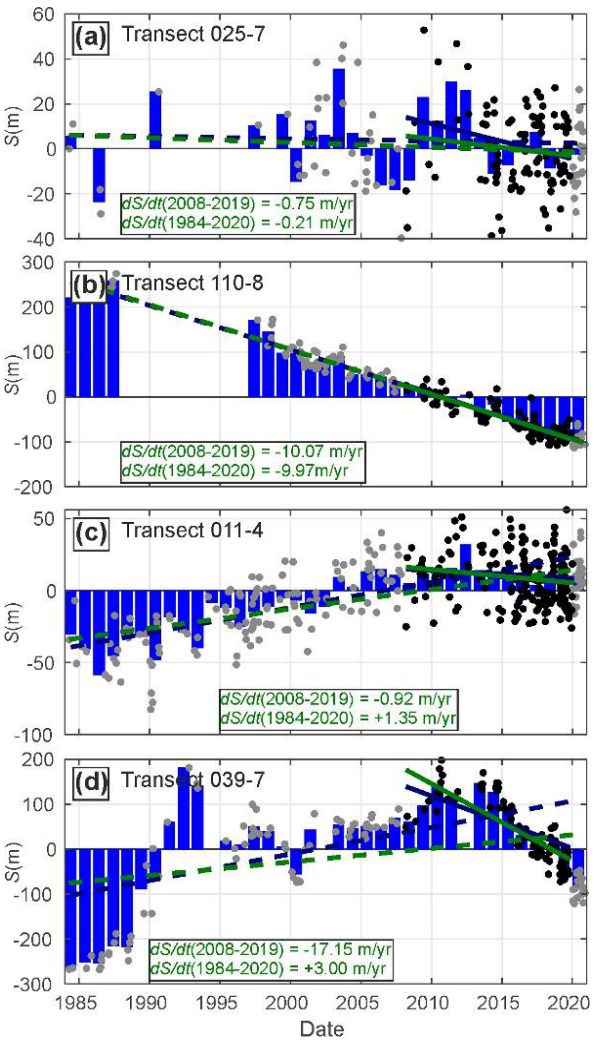

Figure 4. Time series of SDS position deviation from the mean at different representative transects along the coast (a) 025-7 south of Contis, (b) 110-8 near the southern tip of Oléron Island, (c) 011-4 immediately to the north of the Adour estuary training wall and (d) 039-7 between Biscarrosse and the Arcachon Lagoon inlet. In each panel blue bars show yearly mean (S_y) and the dots show individual (S) shoreline data (grey <2008, black ≥2018). The dotted (solid) lines depict the long-term trend dS/dt (in green) (dS_y/dt (in dark blue)) computed on the entire 1984-2020 (limited 2008-2019) period, with the 2008-2019 period corresponding to the available *in situ* data collected for validation. Raw shoreline trend values dS/dt are given in each panel.

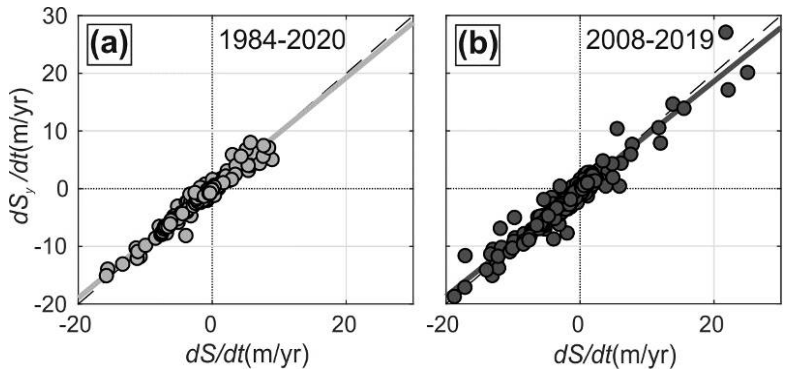

Figure 5. Long-term shoreline trend computed using yearly-mean shoreline dS_y/dt versus that computed using raw shorelines dS/dt over the (a) 1984-2020 and (b) 2008-2019 periods

In order to validate the SDS trends, we used the field dataset described in Nicolae Lerma et al. (2022) collected by the Observatoire de la Côte de Nouvelle-Aquitaine (OCNA) between 2008 and 2019 and we computed the SDS trends over the same period. The dataset consists of 11 years of beach-dune profiles along 41 transects surveyed yearly in spring between the Adour River mouth in the south, and the Gironde estuary mouth in the north (Figure 6a,b), completed by interspersed autumn LiDAR surveys (2014, 2016, 2017, 2018, 2019). The *in situ* shoreline S_{OCNA} was extracted from this dataset as the intersection of the beach-dune profile with elevation $z = 6$ m NGF, which roughly corresponds to the time and space average dune foot elevation along the coast (Nicolae Lerma et al., 2019). Figure 6b shows the comparison between observed trend dS_{OCNA}/dt and SDS trend dS/dt and its 2500-m moving average $\overline{dS/dt}$. Trends are in fair agreement, with RMSE 1.61 m/yr and R^2 = 0.54 for the raw trends (dS/dt, Figure6c), and RMSE = 1.05 m/yr and R^2 = 0.64 for its 2500-m moving average ($\overline{dS/dt}$, Figure 6d). It is important to note that: (1) S_{OCNA} and S are not based on the same shoreline proxy and thus trends are not robustly comparable ; (2) S_{OCNA} is collected at single transects and is thus affected by the presence of alongshore-non uniform features such as megacusp embayments cutting the dune with a cross-shore amplitude locally exceeding 20 m (Castelle et al., 2015), which result in shoreline estimation uncertainties. Additional tests were performed using lower *in situ* shoreline proxies, including the MSL shoreline which should be close to the, time-averaged, SDS proxy. However, the tests showed that the agreement between the trends computed from S_{OCNA}

and S worsens. The two primary reasons are that: (1) the presence of rip channels in the lower profile results in an increased alongshore beach non-uniformity and thus increased S_{OCNA} uncertainties ; (2) beach slope progressively decreases seaward, which also results in more uncertain shoreline detection from the intersection of the beach profile with a given elevation datum. Therefore, the comparison shown in Figure 6 between the trends derived from S and S_{OCNA} (using $z = 6$ m NGF) is fair and can be considered as a validation of our computed SDS trends.

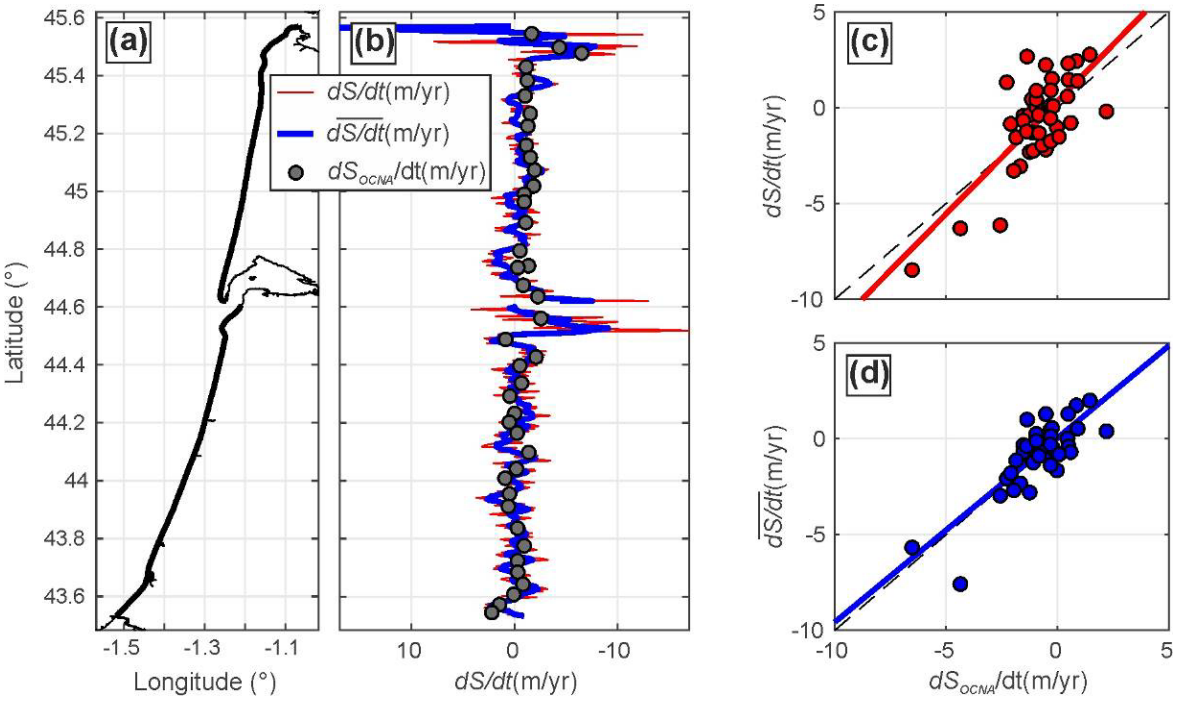

Figure 6. (a) Zoom onto the southern part of the study area where OCNA *in situ* profiles have been collected for validation of shoreline trends, with the thick black shoreline indicating the sections used for analysis. (b) Spatial distribution of 2008-2019 shoreline change trend dS/dt and its 2500-m moving average $\overline{dS/dt}$, with the grey dots showing the measured shoreline trends at the OCNA transects dS_{OCNA}/dt. (c) dS/dt and (d) $\overline{dS/dt}$ versus dS_{OCNA}/dt.

3.3 *Wave data, climate indices and longshore drift computation*

We used wave data from a regional wave hindcast (Boudière et al., 2013; Michaud et al., 2015), which showed excellent skill against interspersed buoy measurements (see Castelle et al., 2020 for details). For each box, hourly time series (2012-2020) of wave conditions was extracted at the grid

point the closest to both the box and to the 50-m isobath (cyan dots in Figure 3a). Significant wave height H_s, peak period T_p and angle of incidence θ in water depth $h_0 \approx 50\ \mathrm{m}$ were transformed into wave conditions at breaking H_{sb}, T_{pb}, θ_b in water depth h_b (Figure 7) using the Larson et al. (2010) empirical formula which assumes nearly shore-parallel offshore bathymetric iso-contours. The local orientation of the shoreline baseline-normal transect was used to compute the wave angle at breaking α_b (Figure 7). These breaking wave conditions were used to force an empirical longshore transport model (Kaczmarek et al., 2015) which is based on an estimation of the mean longshore current V:

$$V = 0.25 k_v \sqrt{\gamma g H_{sb}} \sin 2\alpha_b \quad (1)$$

where g is the gravitational acceleration, $\gamma = 0.78$ is the breaker parameter and k_v = 2.9 is a free parameter previously validated in the north of the study area (Bertin et al., 2008). The longshore sand transport Q_{lst} is then computed at each wave time step depending on $H_{sb}^2 \mathrm{V}$ as:

$$Q_{lst} = 0.23 H_{sb}^2 \mathrm{V}, \text{ if } H_{sb}^2 \mathrm{V} < 0.15 \quad (2)$$

$$Q_{lst} = 0.2300225 + 0.008 H_{sb}^2 \mathrm{V}, \text{ if } H_{sb}^2 \mathrm{V} > 0.15 \quad (3)$$

Hourly hindcast (2012-2020) Q_{slt} was then time averaged for each transect to compute the spatial distribution of the longshore drift Q_s. Alongshore gradients of Q_s are then computed and further compared with shoreline trends dS/dt.

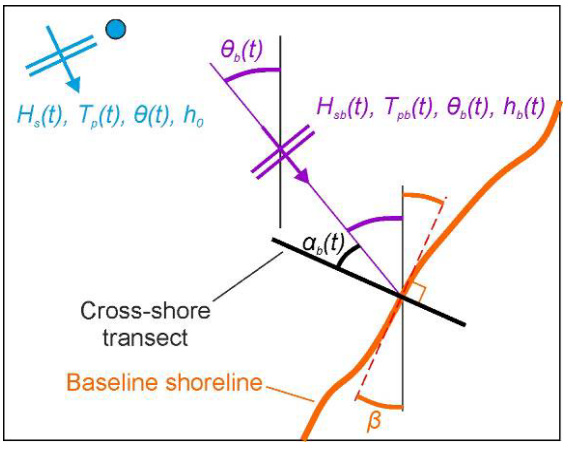

Figure 7. Schematics of longshore drift computation approach: wave hindcast data (H_s, T_p, θ) in water depth $h_0 \approx 50$ m are transformed into breaking wave conditions ($H_{sb}, T_{pb}, \theta_b, h_b$) using Larson et al. (2010) from which breaking wave angle to the shore α_b can be computed according to local transect orientation.

Correlation between SDS interannual variability and large-scale climate modes of atmospheric variability was also explored. Previous work indicates that the winter (DJFM) West Europe Pressure Anomaly (WEPA, Castelle et al., 2017b), defined as the normalised gradient of sea-level pressure between Valentia (Ireland) and Santa Cruz de Tenerife (Canary Islands, Spain) stations, is the primary climate index explaining the interannual variability of e.g. winter wave activity, beach volume changes, precipitation and river discharge in the Bay of Biscay (e.g. Dodet et al., 2019; Jalon-Rojas et al., 2021). A positive winter WEPA corresponds to an intensified and southward shifted Icelandic low / Azores high dipole driving severe storms funnelling high-energy waves towards the west coast of Europe southward of 52° N down to the Moroccan coat (Castelle et al., 2017b, Malagon et al., 2017). The normalised 1942-2020 WEPA time series was computed from *in situ* sea level pressure data measured at the Valentia and Santa Cruz de Tenerife weather stations. In addition, winter-mean values of the conventional teleconnection indices in this region of the world, North Atlantic Oscillation (NAO), Scandinavia (SCAND) and East Atlantic (EA) indices, were also used here. These climate indices, which represent primary intrinsic modes of variability in atmospheric circulation, are derived from rotated EOF analysis of the monthly mean standardized 500-mb height anomalies hindcast in the Northern Hemisphere (Barnston and Livezey, 1987). Amongst these three indices, the NAO has long been known to be the dominant mode of variability in the North Atlantic climate (Hurrel, 1995). Similar to WEPA, a positive NAO reflects an intensified Icelandic low / Azores high dipole, but without southward shift, which limits its influence on winter wave energy in the Bay of Biscay (Castelle et al., 2017b). These indices were downloaded from the National Oceanic and Atmospheric Administration (NOAA) Climate Prediction Centre (www.cpc.ncep.noaa.gov).

4. Results

4.1 *Spatial distribution of shoreline change trends and gradients in longshore drift*

Figure 8 shows the spatial distribution shoreline change rate over the period 1984-2020 along 269 km of sandy shoreline (Figure 8a). Shoreline change rate shows a large spatial variability (Figure 8b,c) with, on average, the shoreline eroding by 0.55 m/yr. The 2500-m moving average shoreline change rate $\overline{dS/dt}$ peaks at 6.94 m/yr (accretion near Verdon, Figure 1a) and drops to 15.61 m/yr (erosion at Gatseau sandspit, Figure 1a), with the largest changes observed along coasts adjacent to inlet and estuary mouths, although with contrasting patterns depending on both the inlet/estuarine system and downdrift or updrift location (Figure 8b,c). Shoreline standard deviation around the long-term trend σ_s is also maximised near inlets and estuary mouths (Figure 8d,e), further indicating that shoreline interannual variability is the largest in these sectors.

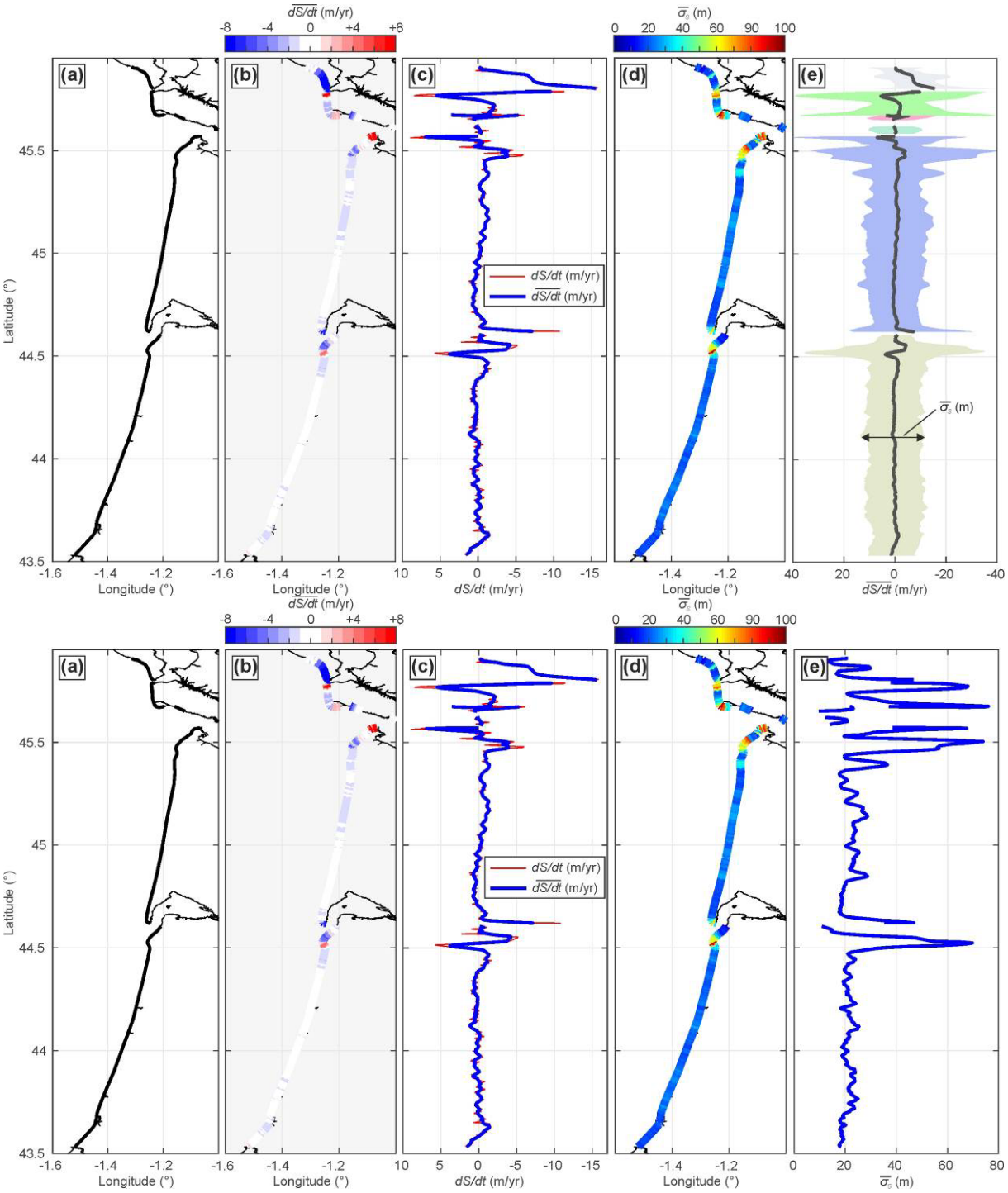

Figure 8. 1984-2020 SDS statistics: (a) Sandy shoreline used in the analysis (thick black line); (b) 2500-m moving averaged shoreline change trend $\overline{dS/dt}$ coloured; (c) raw shoreline change trend (thin red, dS/dt) and its 2500-m moving average (thick blue, $\overline{dS/dt}$); (d) 2500-m moving averaged shoreline standard deviation around the trend $\overline{\sigma_S}$; (e) $\overline{\sigma_S}$.

342 The relationship between long-term shoreline change rate and longshore drift gradient was explored.
343 In some of the areas adjacent to tidal inlets and estuary mouths, the presence of ebb tidal shoals and
344 swash bars deeply affects the incident wave field and, in turn, breaking wave conditions. For such
345 regions the underlying assumptions of the Larson et al. (2010) empirical formula are not tenable.
346 Accordingly, the longshore drift computation and subsequent longshore drift analysis were restricted
347 to the coastline shown in Figure 10a. The latitudinal distribution of shoreline change rate $\overline{dS/dt}$,
348 longshore drift Q_s and gradient of longshore drift dQ_s/dx are shown in Figures 10b, 10c and 10d,
349 respectively. Consistent with previous work (Idier et al., 2013), the longshore drift is mainly directed
350 southwards, except locally at northwest-facing sectors. The resulting gradients are weak, except
351 where shoreline orientation varies substantially, i.e. near inlets and estuary mouth (Figure 10d).
352 Figure 10e-h shows that along the southern coast of Oléron island (Figure 10e) and the Gironde coast
353 (Figure 10g), where some of the largest shoreline trends are observed, there is a statistically
354 significant relationship (p-value < 0.05) between $\overline{dS/dt}$ and dQ_s/dx ($R^2 = 0.92$ and $R^2 = 0.50$,
355 respectively). Along the Landes coast (Figure 10h) the southerly longshore drift is quasi-homogenous
356 (Figure 10c,d), resulting in a mostly stable shoreline position, and thus a weak correlation between
357 $\overline{dS/dt}$ and dQ_s/dx. Despite the statistical relationships are much weaker in Figure 10f,h, similar
358 linear relationships are found with $\overline{dS/dt} \approx 7.10^{-3} dQ_s/dx$ for the four sub-sectors, which will be
359 further discussed in Section 5.

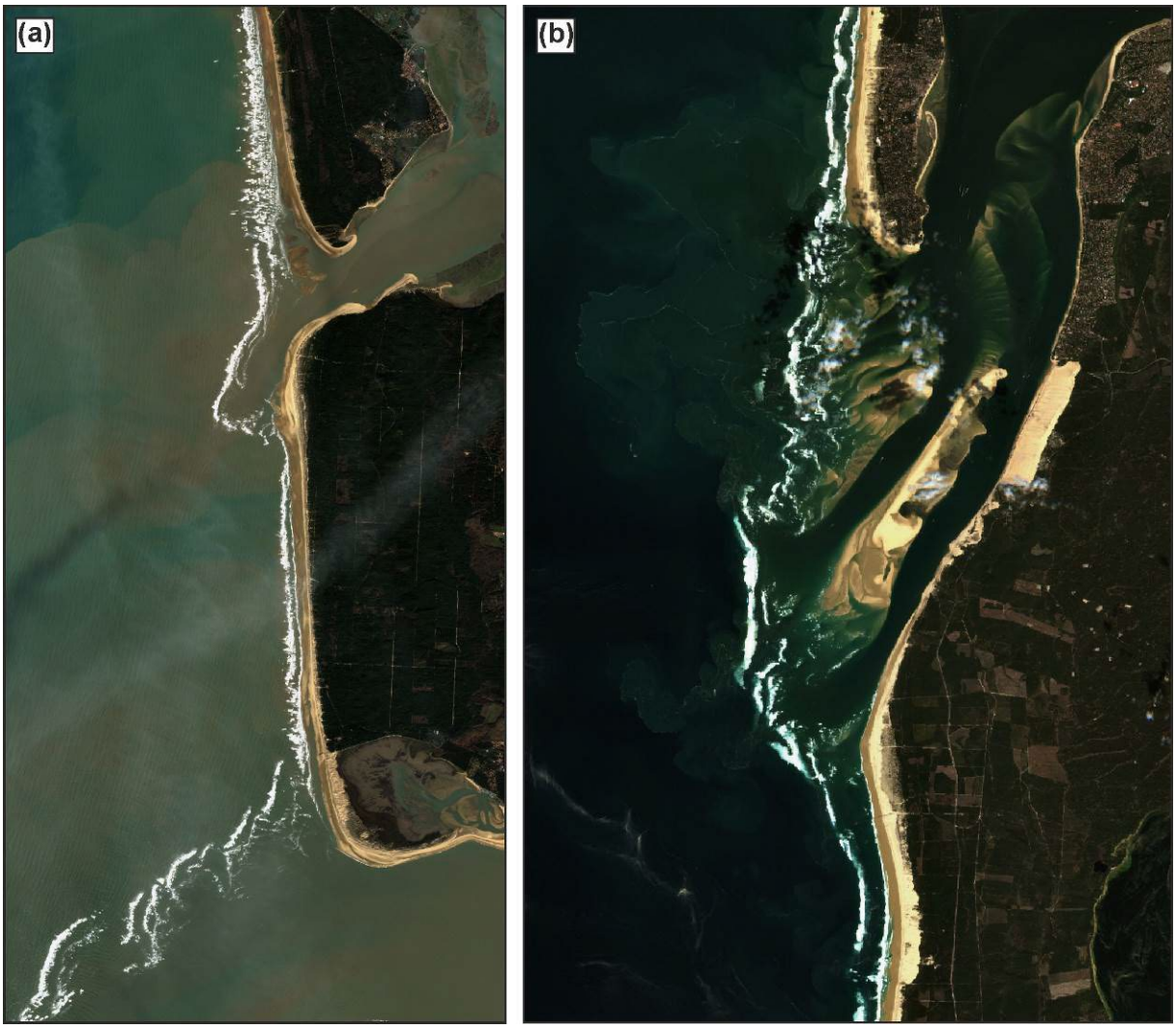

Figure 9. Satellite images showing complex offshore wave transformation and breaking wave patterns around (a) Maumusson inlet (S2 image on January 24, 2019) and (b) Arcachon Lagoon inlet (S2 image on April 19, 2018).

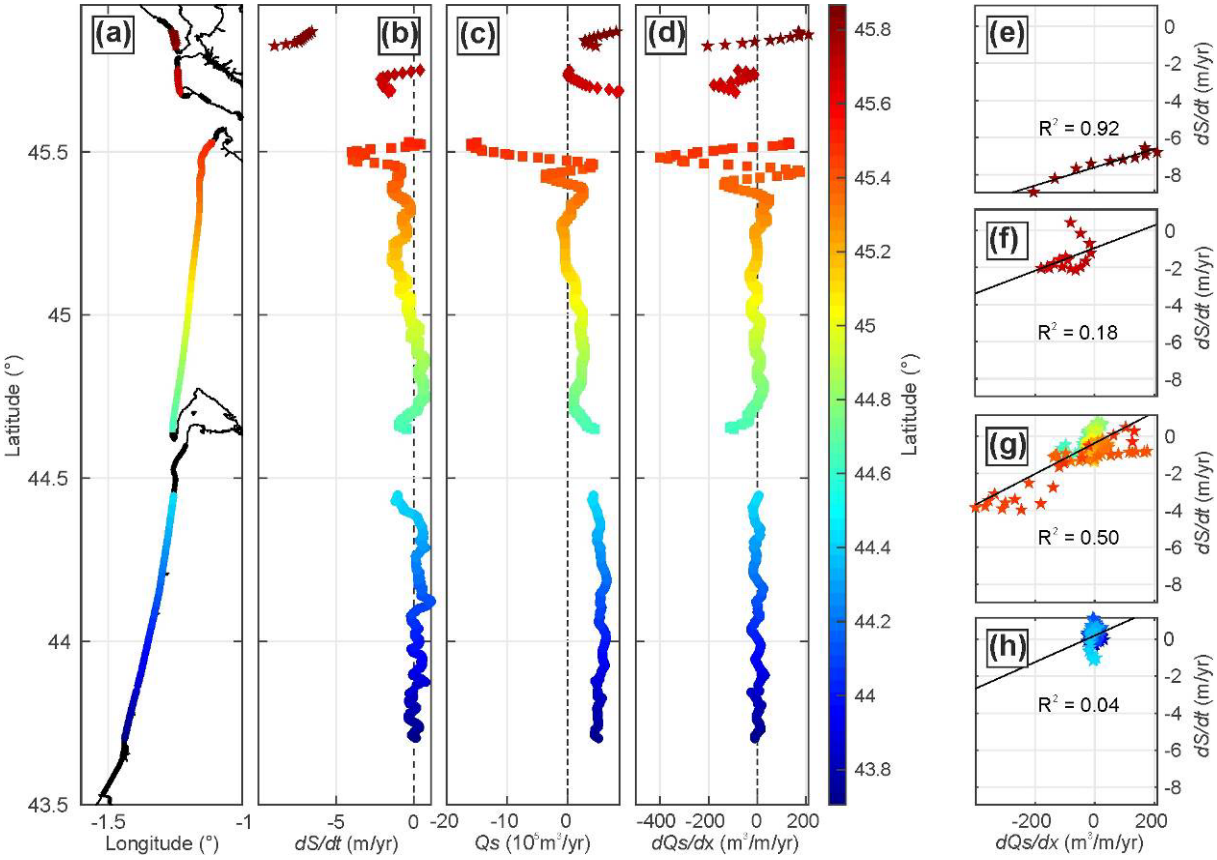

Figure 10. 1984-2020 SDS change trends and longshore drift characteristics: (a) shoreline sectors addressed here; (d) 2500-m moving average shoreline trend $\overline{dS/dt}$ (c) computed longshore drift Q_s (negative southwards) and (d) its alongshore gradients dQ_s/dx; (e-h) $\overline{dS/dt}$ versus dQ_s/dx for the four sub-sectors and corresponding coefficient of determination R^2. Shoreline latitude is coloured in all panels.

4.2 *Time evolution of spatially-averaged shoreline position*

In Section 4.1 we found that the space- and time-averaged erosion along the 269 km of sandy coast is 0.55 m/yr, however the interannual variability was not explored. Previous work at specific sites along this coast and more broadly along the Atlantic coast of Europe (Dodet et al., 2019) showed large interannual shoreline variability that is well correlated with some climate indices. However, the hypothesis that this can apply to entire stretches of coastline has never been investigated. To further test this hypothesis, we addressed the evolution of the yearly shoreline position around the mean $\bar{S}$, averaged along the entire 269-km coast, and compared it with some dominant winter (DJFM) climate

indices in this region. We used the yearly-mean, and not the mean from April 1 to November 30 which would be more consistent to address the impact of winter wave conditions on shoreline change, because some existing shoreline datasets are based on yearly composites (Luijendijk et al., 2018). This approach is also supported by the fact that most of the cloud-free satellite images in southwest France are collected in spring-summer-fall. This is shown in Figure 11 that displays the monthly percentage of satellite images used over 1984-2000, with 82% of the yearly SDS data collected between April 1 and November 30. The yearly mean shoreline is therefore close to the AMJJASON mean shoreline position. The yearly mean shorelines were systematically computed at each transect, with their 1984-2021 average further removed to obtain yearly shoreline position around the mean $\tilde{S}$. The time series of $\tilde{S}$ averaged along the entire 269-km coast is shown in Figure 12c. In order to only account for years when enough spatial coverage was obtained, we computed the yearly percentage N of transects where SDS data are available showing that years with consistently $N > 90\%$ are from 1999 onwards (Figure 12a). However, it is important to note that the space-averaged number of available images per year N_y has varied quite a lot over the years (Figure 12b) depending on the ongoing Earth observation missions, with a dramatic increase since 2016 thanks to Sentinel-2 mission. Hereafter the 1999-2020 $\tilde{S}$ time series is thus used to explore the correlation between climate indices and shoreline response.

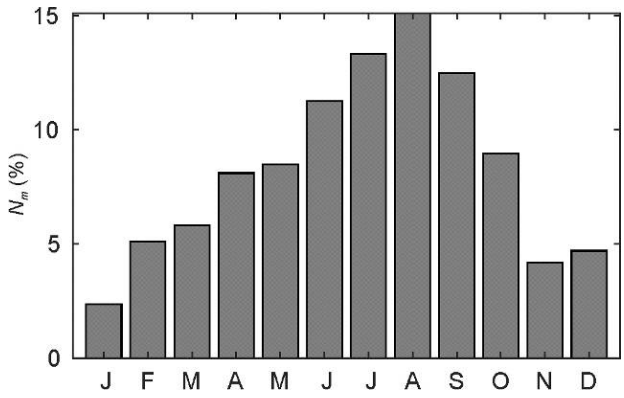

Figure 11. Percentage of SDS data available per month N_m computed over 1984-2020 in southwest France.

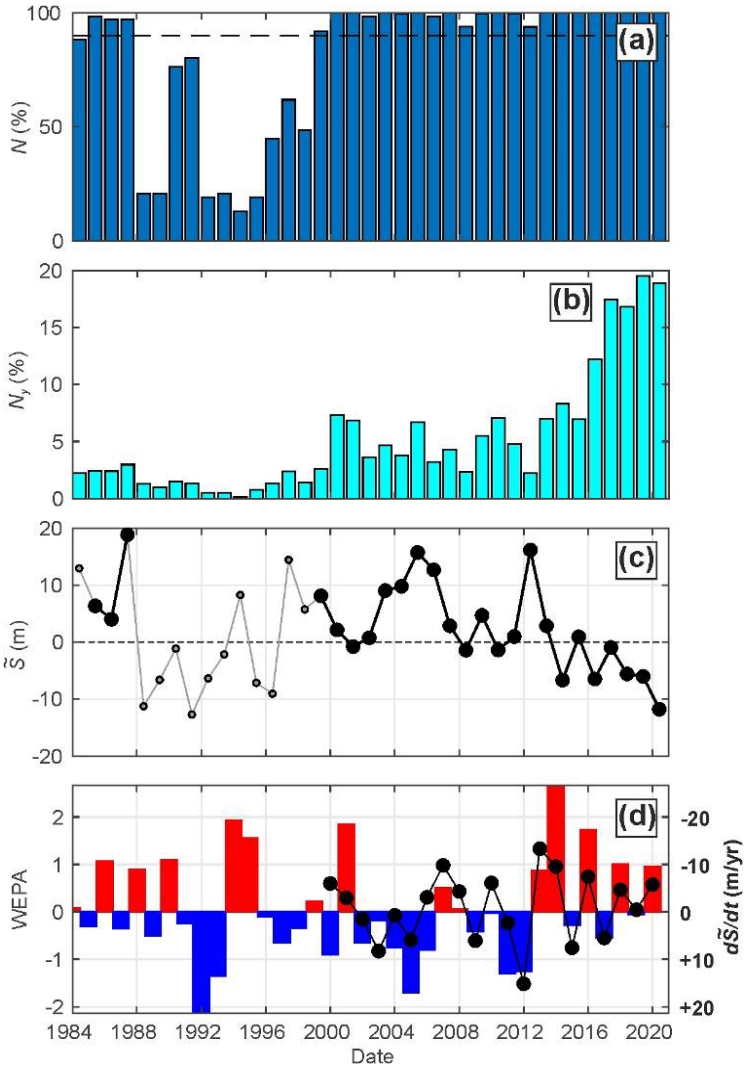

398

399 Figure 12. Time series of (a) yearly percentage N of transects where SDS data are available; (b) space-
400 averaged (along the entire sandy coast, Figure 8a) number of available SDS data N_y, (c) space-
401 averaged (along the entire sandy coast, Figure 8a) yearly-mean shoreline deviation from the mean $\tilde{S}$,
402 with the thick black dots indicating years with $N > 90\%$; (d) winter WEPA climate index (coloured
403 bars) and superimposed $d\tilde{S}/dt$ (black dots) since 1999 showing a coefficient of determination
404 $R^2 = 0.42$. Note that in (d) the $d\tilde{S}/dt$ axis is flipped, with positive WEPA generally driving shoreline
405 erosion ($d\tilde{S}/dt$<0)

406 Figure 12d shows a relationship between $d\tilde{S}/dt$ and WEPA over 1999-2020, with $R^2 = 0.42$, and
407 with erosion (accretion) observed for positive (negative) WEPA. A similar analysis was performed for
408 the other climate indices (not shown) indicating poorer correlation, with by decreasing skill EA (R^2 =

409 0.25), NAO (R^2 = 0.04) and SCAND (R^2 = 0). A closer inspection of the link between WEPA and
410 $d\tilde{S}/dt$ in Figure 12d suggests that the relationship increases when considering more recent periods
411 as the number of available images increases (Figure 12b) and higher resolution (10 m) satellites
412 operate (L8, S2).

413 Figure 13 further demonstrates this increase in correlation between SDS interannual change and
414 winter climate indices by computing correlation between t_0 and 2020, with varying t_0. Correlation is
415 systematically statistically significant and the largest with WEPA, once again followed by EA and NAO,
416 and with SCAND systematically showing poor correlation ($R^2 < 0.2$). In addition R^2 systematically
417 increases with increasing t_0 which is in line with the hypothesis of larger correlation in recent years
418 with more and higher quality images. Importantly, between 2014 and 2020 ($t_0 = 2014$), $R^2 = 0.84$,
419 meaning that WEPA explains more than 80% of the observed space-averaged SDS interannual
420 response in southwest France.

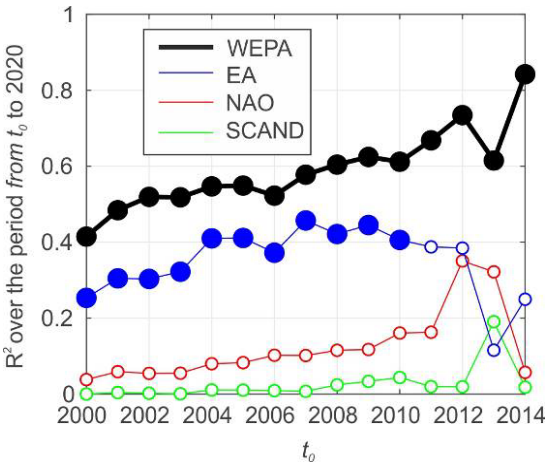

421

422 Figure 13. Coefficient of determination R^2 between yearly-mean shoreline deviation from the mean
423 change $d\tilde{S}/dt$ and different climate indices computed between t_0 (varied) and 2020. Thick filled
424 circles indicate correlation statistically significant correlation ($p < 0.05$).

425 This space-averaging of the yearly shoreline response masks a considerable alongshore variability.
426 This is emphasised in Figure 14 which divides the study area into three zones with contrasting
427 behaviours. North of the Gironde estuary mouth (Figure 14a), the 34-km long sector shows a time-

and space-averaged erosion of 3.05 m/yr with superimposed moderate (10-20 m amplitude) interannual variability linked with WEPA ($R^2 = 50$ over 1999-2020, Figure 14b). Further south, the Gironde coast between the Gironde estuary in the north and Biscarrosse in the south (Figure 14c) shows moderate erosion (0.62 m/yr) with large (20-30 m amplitude) interannual variability also linked with WEPA ($R^2 = 48$ over 1999-2020, Figure 14d). Further south, the Landes coast (Figure 14e) shows a stable shoreline ($d\tilde{S}/dt$ = 0, Figure 14f) with moderate interannual variability (10-20 m amplitude). Such alongshore variability will be further discussed in Section 5.

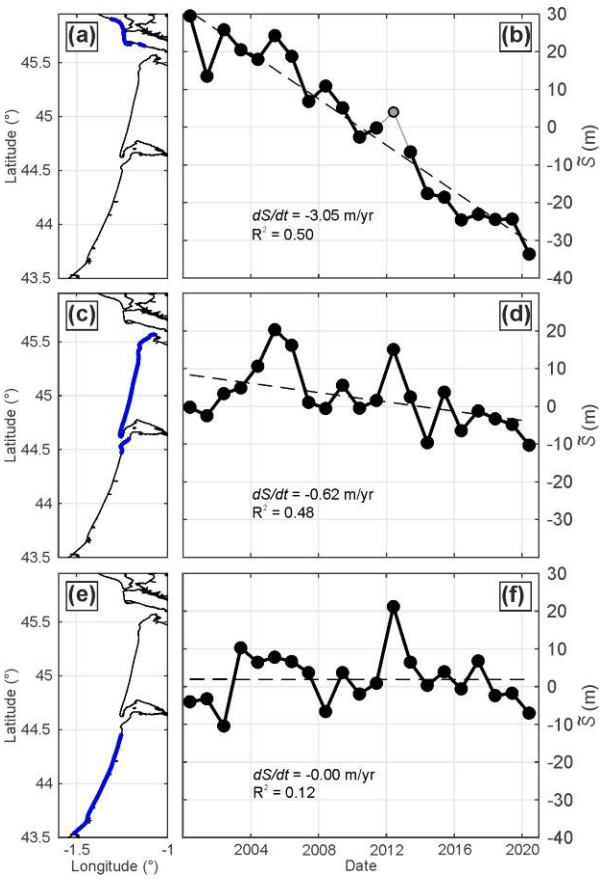

Figure 14. Left-hand panels: sectors (thick blue line) and in the right-hand panels their corresponding space-averaged yearly-mean shoreline deviation from the mean $\tilde{S}$, with the thick black dots indicating years with $N > 90\%$. In the right-hand panels the dotted black line is the long-term (20-yr) trend ($d\tilde{S}/dt$) and R^2 the coefficient of determination with winter WEPA over 1999-2000. (a,b) Charente-Maritime coast; (c,d) Gironde coast; (e,f) Landes coast.

5. Discussion and conclusions

Our SDS analysis (Figure 8) shows an overall eroding sandy coast with maximum shoreline evolutions located along sectors adjacent to the inlets and to the estuary mouth, where erosion and accretion alternate over time on the timescale of decades with an amplitude of 100s of metres. This is consistent with previous work based on historical orthophotos back to the 50s (Bernon et al., 2016; Castelle et al., 2018a). The time- and space-average shoreline evolution between 1984 and 2020 indicates an overall erosion by 0.55 m/yr, which is half of the rate computed in Castelle et al. (2018a) between 1950 and 2014. However, in Castelle et al. (2018a) more than the half of the (stable) Landes coast was disregarded due to the absence of data in the 50s. Disregarding such sector in our SDS dataset shows an erosion of 0.7 m/yr, which is still under that computed over 1950-2014 in Castelle et al. (2018a), but closer to that computed between 1985 and 2014 (0.98 m/yr) in the same paper. The remaining difference may be explained by the uncertainties in both methods. Sea level rise (SLR) alone does not seem to explain such chronic large-scale erosion. For instance the Bruun rule (Bruun, 1962), which is reasonable to apply along this coastline consisting of large beach-dune system with large accommodation space, predicts a SLR-driven shoreline retreat of approximately 0.14 m/yr using a SLR of 3.31 mm/yr over the last two decades and an active profile slope of 0.0235 according to D'Anna et al. (2020). The statistically significant increase of winter-mean wave height in this region associated with increased WEPA and NAO (Castelle et al., 2018b) can explain this larger observed erosion rate. Large-scale coastal sediment budget (Rosati, 2005), including variation in sediment supply by the rivers and the shelf, appears as another candidate to explain such long-term and large-scale erosive trend.

Long-term shoreline trend shows large spatial variability (Figure 8). Away from the tidal inlets and estuary mouths and away from stable sectors (e.g. the Landes coast in Figure 10h), long-term shoreline trends are fairly well correlated with the computed gradients in longshore drift with $\overline{dS/dt} \approx 7.10^{-3} dQ_s/dx$ (Figure 10). Following the one-line assumption that, on the long term, the profile translates parallel to itself without changing shape and with the longshore sand transport taking place uniformly over the entire beach profile from the depth of closure to the top of the dune,

the conservation of sediment gives $dS/dt = (1/h)dQ_s/dx$, with h the height of the active profile. Our computations therefore suggest an active profile height of approximately 142 m, which is much larger than that estimated at e.g. Truc Vert (around 37 m, D'Anna et al., 2021). Such difference may come from an overestimation of the longshore drift magnitude by a factor ≈ 4, which is unlikely given that our values are in line with previous work building on other empirical longshore transport formula (Idier et al., 2013). Another more plausible explanation is that other processes are at work, such SLR-driven erosion, sediment supply and others implying a source/sink term such as $dS/dt = \left(\frac{1}{h}\right)\left(\frac{dQ_s}{dx} + q\right)$. Estimating such, space- (and potentially time-) varying q or any other plausible hypothesis is out of scope.

Despite SDS are associated with relatively large uncertainties in meso-macrotidal high-energy environments (Castelle et al., 2021), space averaging allowed unravelling different yearly shoreline response modes and the links with large-scale climate patterns of atmospheric variability (Figures 12, 13 and 14). Consistent with earlier work on specific sites along the Atlantic coast of Europe (e.g. Castelle et al., 2017a; Burvingt et al., 2018; Dodet et al., 2019), interannual shoreline variability is well correlated with winter WEPA climate index. During the positive phase of WEPA, which reflects an intensified and southward shifted Icelandic low / the Azores dipole funnelling higher energy waves towards western Europe, erosion is observed (Figure 11c). The other teleconnection patterns explain only a little amount of the SDS interannual variability, with the notable exception of EA which can explain up to 40% (Figure 13). This is not surprising as the SLP-based WEPA index contains some variability of EOF-based teleconnection patterns (Scott et al., 2021), primarily NAO and EA which explain 8% and 36% of WEPA variability (Castelle et al., 2017b). Interestingly enough, in contrast with many *in situ* monitoring programs that have demonstrated the dramatic erosion caused by the winter of 2013/2014 (e.g. Blaise et al., 2015; Masselink et al., 2016; Pye and Blott, 2016; Burvingt et al., 2018; Garrote et al., 2018), the space-averaged SDS erosion during that winter is limited (Figures 12c and 14). An explanation is that the SDS proxy, given that images taken at all tidal stages were

considered, is around the intersection of the beach profile with mean sea level elevation. As shown by the bimonthly beach monitoring program at Truc Vert, the impact of the 2013/14 winter was mostly observed at the dry beach and embryo dune with limited impact in the lower intertidal domain (Castelle et al., 2020, their figure 3 at Truc Vert, see also Nicolae Lerma et al., 2019). Limiting satellite images to higher water levels should make the 2013/14 winter impact standing up, as evidenced at Truc Vert using only near high-tide data (Castelle et al., 2021, their figure 10).

In our study WEPA explain > 40% of the interannual space-averaged shoreline variability over 1999-2000, a statistical relationship increasing when considering more recent periods (> 80% over 2014-2020) when the amount and quality of satellite images have both increased. In addition, over the last decade, the predominantly positive winter WEPA including some extremes like in 2013/14 (Figure 11c) clearly resulted in an increased erosion with, on average, the shoreline retreating by over 20 m between 2012 and 2020 (Figure 11b). This may suggest that, in addition to SLR and large-scale sediment budget (Bruun, 1962; Rosati, 2005; Cooper et al., 2020), changes in the pattern and magnitude of winter wave height interannual variability may also impact long-term shoreline variability. This must be investigated on a longer term as such response may just be a cross-shore readjustment of the overall profile. Overall, such links between SDS interannual variability and climate indices calls for more research on the impact of climate change on wave height trends (Hemer et al., 2013; Morim et al., 2019, 2021) and on the climate modes of atmospheric variability (Smith et al., 2019, 2020).

The space averaging of SDS has already been found to provide unprecedented global insight into regional variability of long-term shoreline trends (Luijendijk et al., 2018). We advocate that the pursuing collection of free and publicly-available Landsat and Sentinel 10-m imagery in the next years and decades will make possible an accurate global assessment of the links between the dominant modes of climate variability on shoreline response globally, similar to what has been done for e.g. wave height (e.g. Shimura et al., 2013).

Figure 14 showed that the study area can be further divided into different sectors, revealing different long-term SDS trends and different relationships between winter WEPA and interannual SDS variability. To provide more insight into such alongshore variability in the correlation between climate indices and shoreline response, Figure 15 shows a similar analysis but with all climate indices (WEPA, NAO, EA and SCAND) and by applying a 20-km SDS moving averaged window over the period 1999-2020. It confirms that WEPA is the dominant climate index in explaining shoreline interannual variability along most of the coast, followed by EA and well after NAO and SCAND. Results also show that correlation with WEPA (and the other indices) dramatically drops downdrift of the Gironde estuary mouth and Arcachon inlet, which is not observed updrift. This suggests that, along *O*(1-10 km) of coast downdrift of large-scale inlets and estuary mouths, shoreline response is controlled by factors internal to the estuary mouth / inlet system such as quasi-cyclic ebb-tidal delta dynamics from the timescales of months to years and decades (Cayocca, 2001; Ridderinkhof et al., 2016; Weidman and Ebert, 1993; Burvingt et al., submitted). Along the rest of the coast, even updrift fairly close to the inlet or estuary mouth, the shoreline interannual variability superimposed onto the long-term trend is controlled by factors external to the system which are primarily the variability in winter-mean wave height correlated to winter WEPA index. Noteworthy, less uncertain SDS data (e.g. through tide and/or runnup correction, Vos et al., 2019a, 2020; Castelle et al., 2021) should result in more accurate correlations with the climate indices. Castelle et al. (2021) showed that, at Truc Vert beach in southwest France, interranual shoreline change correlation with WEPA increases by nearly 60% using tide and runup correction. We hypothesize that such correction could allow narrowing the moving average window and thus provide higher spatial resolution information on shoreline response. For instance, it could be used to address in more detail the internal – external control transition at the updrift sectors of the estuary and inlet mouths that is hypothesized to occur at a short (e.g. a few kilometres) distance from the mouth.

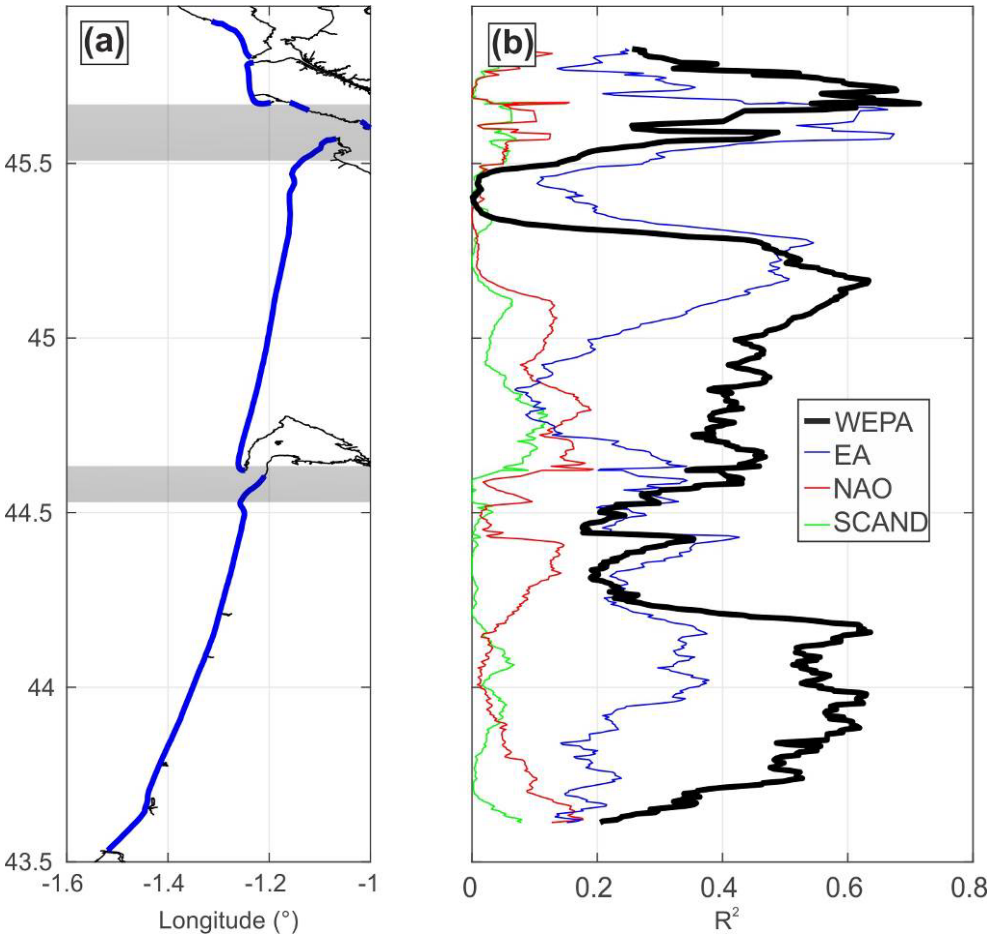

542

543 Figure 15. (a) Shoreline sector addressed here (thick blue line); (b) coefficient of determination R^2
544 between, 10-km moving averaged, yearly-mean shoreline deviation from the mean change $d\tilde{S}/dt$
545 and different climate indices on the period 1999-2020.

546 The SDS analysis provided new insight into shoreline response and the primary drivers, which can
547 guide future numerical model application. For instance, we hypothesize that reduced complexity
548 models coupling cross-shore and longshore processes (e.g. Vitousek et al., 2017b; Robinet et al.,
549 2018; Antonilez et al., 2019) can be applied and further used for future shoreline prediction well
550 away from the downdrift zones of the major inlets and estuary mouths. Such models can then be
551 used to estimate sediment sources and sink through calibration with SDS. Further, prediction of
552 future shoreline change and their uncertainties will be made possible using a similar approach as
553 D'Anna et al. (2021).

A similar SDS analysis can be performed along any coastline in the world in order to guide future model development and application. In this frame, SDS are also a promising input for coastal modelling through data assimilation (Turner et al., 2021). We advocate that, by keeping the reduced-complexity model 'on the track', data assimilation will allow: (1) to both identifying the primary sources of model errors and understanding the links between time-varying free parameters and changes in environmental conditions but also (2) to impose shoreline boundary conditions at inlets and estuary mouths during hindcast thus extending their range of application.

Acknowledgments

This work was done in the framework and funded by Agence Nationale de la Recherche (ANR) grant number ANR-21-CE01-0015. The *in situ* date used for the validation of SDS trends was collected and provided by the Observatoire de la Côte de Nouvelle-Aquitaine (OCNA). NORGAS-UG wave hindcast data provided by LOPS-Ifremer. EOF-based climate indices used in this study are publicly available for the period 1980–2017 (National Oceanic and Atmospheric Administration (NOAA) Climate Prediction Center; www.cpc.ncep.noaa.gov). We thank Kilian Vos and the Water Research Laboratory for developing and making freely available the CoastSat toolkit.

References cited

Antolínez, J.A.A., Méndez, F.J., Anderson, D., Ruggiero, P., Kaminsky, G.M., 2019. Predicting climate driven coastlines with a simple and efficient multi-scale model. Journal of Geophysical Research Earth Surface, 124, doi:10.1029/2018JF004790.

Barnston, A. G., Livezey, R.E., 1987. Classification, seasonality and persistence of low-frequency atmospheric circulation patterns. Monthly Weather Review, 115(6), 1083–1126, doi:10.1175/1520-0493(1987)115<1083:csapol>2.0.co;2.

Bernon, N., Mallet, C., Belon, R., 2016. Caractérisation de l'aléa recul du trait de côte sur le littoral de la côte aquitaine aux horizons 2025 et 2050. BRGM Report RP-66277-FR, 99 pages, in French.

578 Bertin, X., Castelle, B., Chaumillon, E., Butel, R., Quique, R., 2008. Longshore drift estimation and
579 inter-annual variability at a high-energy dissipative beach: st. Trojan Beach, SW Oleron Island,
580 France. Continental Shelf Research, 28, 1316-1332.
581 Biausque, M., Senechal, N., 2019. Seasonal morphological response of an open sandy beach to winter
582 wave conditions: The example of Biscarrosse beach, SW France. Geomorphology, 332, 157-
583 169.
584 Bishop-Taylor, R., Sagar, S., Lymburner, L., Alam, I., Sixsmith, J., 2019. Sub-pixel waterline extraction:
585 characterising accuracy and sensitivity to indices and spectra. Remote Sensing, 11, 2984,
586 doi:10.3390/rs11242984.
587 Bishop-Taylor, R., Nanson, R., Sagar, S., Lymburner, L., 2021. Mapping Australia's dynamic coastline
588 at mean sea level using three decades of Landsat imagery. Remote Sensing of Environment,
589 267, 112734, doi:10.1016/j.rse.2021.112734.
590 Blaise, E., Suanez, S., Stephan, P., Fichaut, B., David, L., Cuq, V., Autret, R., Houron, J., Rouan, M.,
591 Floc'h, F., Ardhuin, F., Cancouet, R., Davidson, R., Costa, S., Delacourt, C., 2015. Bilan des
592 tempêtes de l'hiver 2013-2014 sur la dynamique du recul de trait de côte en Bretagne.
593 Geomorphologie: Relief, Processus, Environnement, 21(3), 267–292.
594 Bossard, V., Nicolae Lerma, A., 2020. Geomorphologic characteristics and evolution of managed
595 dunes on the South West Coast of France. Geomorphology, 367, 107312,
596 doi:10.1016/j.geomorph.2020.107312.
597 Boudière, E., Maisondieu, C., Ardhuin, F., Accensi, M., Pineau-Guillou, L., Lepesqueur, J., 2013. A
598 suitable metocean hindcast database for the design of Marine energy converters.
599 International Journal of Marine Energy, 3–4, 40-52, doi:10.1016/j.ijome.2013.11.010.
600 Bruun, P., 1962. Sea-level rise as a cause of shore erosion. Journal of the Waterways and Harbors
601 Division, 88(1), 117–132.

602 Burvingt, O., Masselink, G., Scott, T., Davidson, M., Russell, P., 2018. Climate Forcing of Regionally-
603 Coherent Extreme Storm Impact and Recovery on Embayed Beaches. Marine Geology, 401,
604 112–128.
605 Burvingt, O., Nicolae Lerma, A., Lubac, B., Senechal, N., Mallet, C., submitted. Geomorphological
606 control of sandy beach and dunes alongside a mixed-energy tidal inlet. Marine Geology
607 Castelle, B., Guillot, B., Marieu, V., Chaumillon, E., Hanquiez, V., Bujan, S., Poppeschi, C., 2018a.
608 Spatial and temporal patterns of shoreline change of a 280-km long high-energy disrupted
609 sandy coast from 1950 to 2014: SW France. Estuarine Coastal and Shelf Science, 200, 212–
610 223.
611 Castelle, B., Bujan, S., Ferreira, S., Dodet, G., 2017a. Foredune morphological changes and beach
612 recovery from the extreme 2013/2014 winter at a high-energy sandy coast. Marine Geology,
613 385, 41-55.
614 Castelle, B., Dodet, G., Masselink, G., Scott, T., 2017b. A new climate index controlling winter wave
615 activity along the Atlantic coast of Europe: The West Europe Pressure Anomaly. Geophysical
616 Research Letters, 44 (3), 1384-1392.
617 Castelle, B., Marieu, V., Bujan, S., Splinter, K.D., Robinet, A., Senechal, N., Ferreira, S., 2015. Impact of
618 the winter 2013e2014 series of severe Western Europe storms on a double-barred sandy
619 coast: beach and dune erosion and megacusp embayments. Geomorphology 238, 135-148,
620 doi:10.1016/j.geomorph.2015.03.006.
621 Castelle, B., Masselink, G., Scott, T., Stokes, C., Konstantinou, A., Marieu, V., Bujan, S., 2021. Satellite-
622 derived shoreline detection at a high-energy meso-macrotidal beach. Geomorphology, 383,
623 107707.
624 Castelle, B., Marieu, V., Bujan, S., Ferreira, S., 2020. 16 years of topographic surveys of rip-channelled
625 high-energy meso-macrotidal sandy beach. Scientific Data, 7, 410, doi:10.1038/s41597-020-
626 00750-5.

627 Castelle B, Dodet G, Masselink G, Scott, T., 2018b. Increased winter-mean wave height, variability,
628 and periodicity in the Northeast Atlantic over 1949–2017. Geophysical Research Letters
629 45(8): 3586–3596.
630 Cayocca, F., 2001. Long-term morphological modeling of a tidal inlet: the Arcachon Basin, France.
631 Coast. Eng. 42, 115-142, doi:10.1016/S0378-3839(00)00053-3.
632 Cuttler, M.V.W., Vos, K., Branson, P., Hansen, J.E., O'Leary, M., Browne, N.K., Lowe, R.J., 2020.
633 Interannual Response of Reef Islands to Climate-Driven Variations in Water Level and Wave
634 Climate. Remote Sensing, 12, 4089, doi:10.3390/rs12244089.
635 D'Anna, M., Castelle, B., Idier, D., Le Cozannet, G., Rohmer, J., Robinet, A., 2020. Impact of model free
636 parameters and sea-level rise uncertainties on 20-years shoreline hindcast: the case of Truc
637 Vert beach (SW France). Earth Surface Processes and Landforms, 45(8), 1895-1907,
638 doi:10.1002/esp.4854.
639 D'Anna, M., Castelle, B., Idier, D., Rohmer, J., Le Cozannet, G., Thieblemont, R., Bricheno, L., 2021.
640 Uncertainties in shoreline projections to 2100 at Truc Vert beach (France): Role of sea-level
641 rise and equilibrium model assumptions. Journal of Geophysical Research: Earth Surface, 126,
642 e2021JF006160, doi:org/10.1029/2021JF006160.
643 Davies, H.C., 2015. Weather chains during the 2013/2014 winter and their significance for seasonal
644 prediction. Nature Geoscience, 8, 833–837.
645 Di Luccio, D., Benassai, G., Di Paola, G., Mucerino, L., Buono, A., Rosskopf, C.M., Nunziata, F.,
646 Migliaccio, M., Urciuoli, A., Montella, R., 2019. Shoreline Rotation Analysis of Embayed
647 Beaches by Means of In Situ and Remote Surveys. Sustainability, 11, 725,
648 doi:10.3390/su11030725.
649 Dodet, G., Castelle, B., Masselink, G., Scott, T., Davidson, M., Floc'h, F., Jackson, D.W.T., Suanez, S.,
650 2019. Beach recovery from extreme storm activity during the 2013/14 winter along the
651 Atlantic coast of Europe. Earth Surface Processes and Landforms, 44(1), 393-401.

652 Duarte, C.R., De Miranda, F.P., Landau, L., Souto, M.V.S., Sabadia, J.A.B., Da Silva, C.A., Rodrigues,
653 L.I.D.C., Damasceno, A.M., 2018. Short-time analysis of shoreline based on RapidEye satellite
654 images in the terminal area of Pecem Port, Ceara, Brazil. International Journal of Remote
655 Sensing, 39, 4376-4389.
656 Garrote, J., Díaz-Álvarez, A., Nganhane, H.V., Garzón Heydt, G., 2018. The Severe 2013–14 Winter
657 Storms in the Historical Evolution of Cantabrian (Northern Spain) Beach-Dune Systems.
658 Geosciences 2018, 8, 459, doi:10.3390/geosciences8120459.
659 Hemer, M., Fan, Y., Mori, N., Semedo, A., Wang, X., 2013. Projected changes in wave climate from a
660 multi-model ensemble. Nature Climate Change, 3(5), 471–476, doi:10.1038/nclimate1791.
661 Hurrell, J.W., 1995. Decadal trends in the North Atlantic Oscillation: Regional temperatures and
662 precipitation. Science, 269(5224), 676–679, doi:10.1126/science.269.5224.676.
663 Hzami, A., Heggy, E., Amrouni, O., Mahé, G., Maanan, M., Abdeljaouad, S., 2021. Alarming coastal
664 vulnerability of the deltaic and sandy beaches of North Africa. Scientific Reports, 11, 2320,
665 doi:10.1038/s41598-020-77926-x.
666 Idier, D., Castelle, B., Charles, E., Mallet, C., 2013. Longshore sediment flux hindcast: spatio-temporal
667 variability along the SW Atlantic coast of France. Journal of Coastal Research, 165, 1785-
668 1790, doi:10.2112/SI65-302.1.
669 Jalón-Rojas, I., Castelle, B., 2021. Climate Control of Multidecadal Variability in River Discharge and
670 Precipitation in Western Europe. Water 2021, 13, 257, doi:10.3390/w13030257.
671 Kaczmarek, L.M., Ostrowski, R., Pruszak, Z., Rozynski, G., 2005. Selected problems of sediment
672 transport and morphodynamics of a multi-bar nearshore zone. Estuarine, Coastal and Shelf
673 Science 62, 415–425.
674 Le Cann, B., 1990. Barotropic tidal dynamics of the Bay of Biscay shelf: observations, numerical
675 modelling and physical interpretation. Continental Shelf Research, 10, 723-758,
676 doi:10.1016/0278-4343(90)90008-A.

677 Liu, Q., Trinder, J., Turner, I.L., 2017. Automatic super-resolution shoreline change monitoring using
678 Landsat archival data: a case study at Narrabeen–Collaroy Beach, Australia. Journal of
679 Applied Remote Sensing, 11, 016036, doi:10.1117/1.JRS.11.016036.
680 Luijendijk, A., Hagenaars, G., Ranasinghe, R., Baart, F., Donchyts, G., Aarninkhof, S., 2018. The State
681 of the World's Beaches. Scientific Reports, 8(1), doi:10.1038/s41598-018-24630-6.
682 Malagon Santos, V., Haigh, I.D., Thomas, W., 2017. Spatial and temporal clustering analysis of
683 extreme wave events around the UK coastline. Journal of Marine Science and Engineering,
684 5(3), 28. Doi:10.3390/jmse5030028. Masselink, G., Castelle, B., Scott, T., Dodet, G., Suanez,
685 S., Jackson, D., Floc'h, F., 2016. Extreme wave activity during 2013/2014 winter and
686 morphological impacts along the Atlantic coast of Europe. Geophysical Research Letters, 43,
687 2135-2143, doi:10.1002/2015GL067492.
688 Mazieres, A., Gillet, H., Castelle, B., Mulder, T., Guyot, C., Garlan, T., Mallet, C., 2014. High-resolution
689 morphobathymetric analysis and evolution of Capbreton submarine canyon head (Southeast
690 Bay of Biscay - French Atlantic Coast) over the last decade using descriptive and numerical
691 modeling. Marine Geology, 351, 1-12.
692 Michaud, H., Pasquet, A., Baraille, R., Leckler, F., Aouf, L., Dalphinet, A., Huchet, M., Roland, A.,
693 Dutour-Sikiric, M., Ardhuin, F., Filipot, J.F, 2015. Implementation of the new French
694 operational coastal wave forecasting system and application to a wave-current interaction
695 study. 14th International Workshop on Wave Hindcasting and Forecasting & 5th Coastal
696 Hazard Symposium, Nov. 8-13, Key West, Florida, USA.
697 Montaño, J., Coco, G., Antolínez, J.A.A., Beuzen, T., Bryan, K.R., Cagigal, L., Castelle, B., Davidson,
698 M.A., Goldstein, E.B., Ibaceta, R., Idier, D., Ludka, B.C., Masoud-Ansari, S., Mendez, F.J.,
699 Murray, A.B., Plant, N.G., Ratliff, K.M., Robinet, A., Rueda, A., Sénéchal, N., Simmons, J.A.,
700 Splinter, K.D., Stephens, S., Townend, I., Vitousek, S., Vos, K., 2020. Blind testing of shoreline
701 evolution models. Scientific Reports, 10, 2137, doi:10.1038/s41598-020-59018-y.

Morim, J., Hemer, M., Wang, X. L., Cartwright, N., Trenham, C., Semedo, A., ... & Andutta, F., 2019. Robustness and uncertainties in global multivariate wind-wave climate projections. Nature Climate Change, 9(9), 711-718.

Morim, J., Vitousek, S., Hemer, M., Reguero, B., Erikson, L., Casas-Prat, M., ... & Timmermans, B., 2021. Global-scale changes to extreme ocean wave events due to anthropogenic warming. Environmental Research Letters, 16(7), 074056.

Nicolae Lerma, A., Castelle, B., Marieu, V., Robinet, A., Bulteau, T., Bernon, N., Mallet, C., 2022. Decadal beach-dune profile monitoring along a 230-km high-energy mesotidal sandy coast. Applied Geography, doi:10.1016/j.apgeog.2022.102645.

Nicolae Lerma, A., Ayache, B., Ulvoas, B., Paris, F., Bernon, N., Bulteau, T., Mallet, C., 2019. Pluriannual beach-dune evolutions at regional scale: Erosion and recovery sequences analysis along the Aquitaine coast based on airborne LiDAR data. Continental Shelf Research, 189, 103974.

Oppenheimer, M.B.C., Glavovic, J., Hinkel, R., van de Wal, A.K., Magnan, A., et al., 2019. Sea level rise and implications for low-lying islands, coasts and communities. In H.-O. Portner, D. C. Roberts, V. Masson-Delmotte, P. Zhai, M. Tignor, E. Poloczanska, et al. (Eds.), IPCC special report on the ocean and cryosphere in a changing climate.

Pye, K., Blott, S.J., 2016. Assessment of beach and dune erosion and accretion using LiDAR: Impact of the stormy 2013–14 winter and longer term trends on the Sefton Coast, UK. Geomorphology, 266, 146-167, doi:10.1016/j.geomorph.2016.05.011.

Ridderinkhof, W., Hoekstra, P., van der Vegt, M., de Swart, H.E., 2016. Cyclic behaviour of sandy shoals on the ebb-tidal deltas of the Wadden Sea. Continental Shelf Research, 115, 14-26, doi:10.1016/j.csr.2015.12.014.

Robinet, A., Idier, D., Castelle, B., Marieu, V., 2018. A reduced-complexity shoreline change model combining longshore and cross-shore processes: the LX-Shore model. Environmental Modelling & Software, 109, 1–16, doi:10.1016/j.envsoft.2018.08.010.

728 Rosati, J.D., 2005. Concepts in sediment budgets. Journal of Coastal Research, 212, 307-322,
729 doi:10.2112/02-475A.1.
730 Sánchez-García, E., Palomar-Vázquez, J.M., Pardo-Pascual, J.E., Almonacid-Caballer, J., Cabezas-
731 Rabadán, C., Gómez-Pujol, L., 2020. An efficient protocol for accurate and massive shoreline
732 definition from mid-resolution satellite imagery, Coastal Engineering, 160, 103732,
733 doi:10.1016/j.coastaleng.2020.103732.
734 Scott, T., McCarroll, R. J., Masselink, G., Castelle, B., Dodet, G., Saulter, A., et al. (2021). Role of
735 atmospheric indices in describing inshore directional wave climate in the United Kingdom
736 and Ireland. Earth's Future, 9, e2020EF001625, doi:10.1029/2020EF001625.
737 Shimura, T., Mori, N., Mase, H., 2013. Ocean waves and teleconnection patterns in the Northern
738 Hemisphere. Journal of Climate, 26(21), 8654–8670, doi:10.1175/JCLI-D-12-00397.1.
739 Smith, D.M., Eade, R., Scaife, A.A., Caron, L.P., Danabasoglu, G., DelSole, T.M., et al., 2019. Robust
740 skill of decadal climate predictions. NPJ: Climate and Atmospheric Sciences, 2(13),
741 doi:10.1038/s41612-019-0071-y
742 Smith, D.M., Scaife, A.A., Eade, R., Athanasiadis, P., Bellucci, A., Bethke, I., et al., 2020. North Atlantic
743 climate far more predictable than models imply. Nature, 583(7818), 796–800,
744 doi:10.1038/s41586-020-2525-0
745 Toure, S., Diop, O., Kpalma, K., Maiga, A.S., 2019. Shoreline Detection using Optical Remote Sensing:
746 A Review. ISPRS Int. J. Geo-Inf., 8(2), 75, doi:10.3390/ijgi8020075.
747 Tran, Y.H., Barthélemy, E., 2020. Combined longshore and cross-shore shoreline model for closed
748 embayed beaches. Coastal Engineering, doi: 10.1016/j.coastaleng.2020.103692.
749 Vitousek, S., Barnard, P.L. Limber, P., 2017a. Can beaches survive climate change? Journal of
750 Geophysical Research – Earth Surface, 122, 1060–1067.
751 Vitousek, S., Barnard, P.L., Limber, P., Erikson, L., Cole, B., 2017b. A model integrating longshore and
752 cross-shore processes for predicting long-term shoreline response to climate change. Journal
753 of Geophysical Research Earth Surface 122 (4), 782–806, doi:10.1002/2016JF004065.

754 Vos, K., Harley, M.D., Splinter, K.D., Simmons, J.A., Turner, I.L., 2019a. Sub-annual to multi-decadal
755 shoreline variability from publicly available satellite imagery. Coastal Engineering,
756 doi:10.1016/j.coastaleng.2019.04.004.
757 Vos, K., Splinter, K.D., Harley, M.D., Simmons, J.A., Turner, I.L., 2019b. CoastSat: A Google Earth
758 Engine-enabled Python toolkit to extract shorelines from publicly available satellite imagery.
759 Environmental Modelling & Software, 122, 104528, doi:10.1016/j.envsoft.2019.104528.
760 Vos, K., Harley, M.D., Splinter, K.D., Walker, A., Turner, I.L., 2020. Beach slopes from satellite-derived
761 shorelines. Geophysical Research Letters, 47, doi:10.1029/2020GL088365 e2020GL088365.
762 Vos, K., Harley, M.D., Turner, I.L., Splinter, 2022. Large regional variability in coastal erosion caused
763 by ENSO. https://doi.org/10.21203/rs.3.rs-666160/v1.
764 Weidman, C.R., Ebert, J.R., 1993. Cyclic spit morphology in a developing inlet system. In: Aubrey,
765 D.G., Giese, G.S. (Eds.), Formation and Evolution of Multiple Tidal Inlet Systems, vol. 44.
766 American Geophysical Union, Washington D.C., pp. 158-185